

Probing Molecular Interactions at MXene–Organic Heterointerfaces

Muhammad Boota,* Chi Chen, Long Yang, Alexander I. Kolesnikov, Naresh C. Osti, William Porzio, Luisa Barba, and Jianjun Jiang



Cite This: *Chem. Mater.* 2020, 32, 7884–7894



Read Online

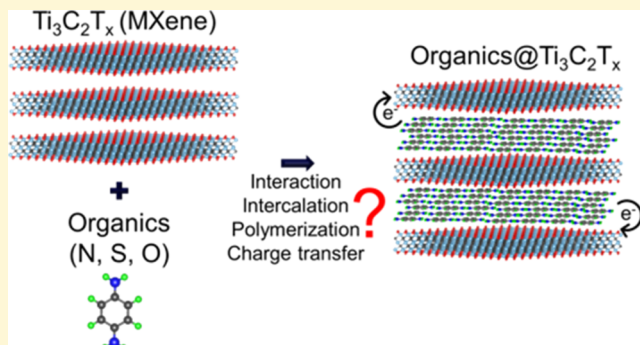
ACCESS |

Metrics & More

Article Recommendations

Supporting Information

ABSTRACT: Here, using a combined theoretical and experimental approach, we have investigated the interaction mechanism of titanium carbide MXene with a variety of organic molecules whose end groups are O, S, N, and tertiary amines. All organic molecules intercalated between MXene layers; however, layer expansion followed the end group of the organic molecules. A broad range of optical spectroscopies confirmed that the nature of interactions/reactions of titanium carbide MXene with organic molecules is also end group-dependent that involve a variety of complex interactions between MXene and organic molecules such as electrostatic interactions, polymerization, strong binding, and in some cases catalytic decomposition of the organic molecules. First-principles calculations revealed that organic molecules tend to stay flat on the MXene surface during molecular assembly and that the binding and charge transfer from organic molecules to MXene occur, which are strongly end group-dependent, corroborating the experimental observations. The impact of interactions/reactions within the MXene–organic heterostructures on pseudocapacitance is further discussed.



INTRODUCTION

Two-dimensional (2D) inorganic heterostructures offer a unique set of properties that make them attractive for a variety of applications such as energy conversion and storage, electronics, water purification, and catalysis.¹ Owing to their inert nature, the majority of 2D inorganic heterostructures are held together by van der Waals forces.¹ Although nature has provided a finite number of inorganic 2D materials, they are growing rapidly from lab to commercial scale (e.g., graphene, metal dichalcogenides, boron nitride, and so forth). In contrast to inorganic materials, organic materials are nearly unlimited that are readily available or can be synthesized with tunable properties.² By precisely integrating organic and inorganic materials at the subnanometer scale, nearly unlimited combinations of organic–inorganic heterostructures can be manufactured.^{1,2} The challenge, however, is that the integration of organic materials with their inorganic counterpart brings a variety of complex interactions (e.g., van der Waals forces, hydrogen bonding, π – π interactions, chemical bonding, and so forth), and understanding the nature of these interactions is a prerequisite to control the end properties of organic–inorganic heterostructures.^{1,2}

Discovered in 2011, MXenes with a general formula of $M_{n+1}X_nT_x$ (M = transition metal, e.g., Ti, V, Mo, Nb; X is C and/or N; T = surface-terminating functionality, O, OH, F, and/or Cl; and $n = 1, 2$, or 3) are a fast-growing family of highly conductive 2D transition metal carbides, nitrides, and carbonitrides.^{3,4} The first reported MXene was $Ti_3C_2T_x$ that

was synthesized by selective extraction of Al from the crystalline MAX phase Ti_3AlC_2 using fluoride-containing acidic solutions.³ Since the discovery of $Ti_3C_2T_x$, more than 30 MXene compositions have been published, and a number of solid solutions have been reported by computational methods.⁵ MXenes offer a unique set of properties including metallic conductivity, high mechanical strength, hydrophilicity, and chemical stability, enabling their use in a variety of applications such as electromagnetic interference shielding,⁶ energy conversion and storage,⁷ optoelectronics,⁸ catalysis,⁹ wireless communication,¹⁰ chemical sensing,¹¹ and others.^{3,5}

Intercalation is considered as a prime modulator that largely governs the properties and applications of MXenes.^{3,5} Intercalation of metal ions and organic molecules have shown promise to expand MXene layers, resulting in better charge transport for improved electrochemical performance in energy storage devices, capacitive deionization, gas sensing, and biomedical applications.^{3,5,12} Previously, intercalation of many organic molecules (e.g., dimethyl sulfoxide, tetrabutylammonium, hydrazine monohydrate, urea, dimethyl formamide, tetrabutylammonium hydroxide, choline hydroxide, *n*-butyl-

Received: June 24, 2020

Revised: August 26, 2020

Published: August 27, 2020



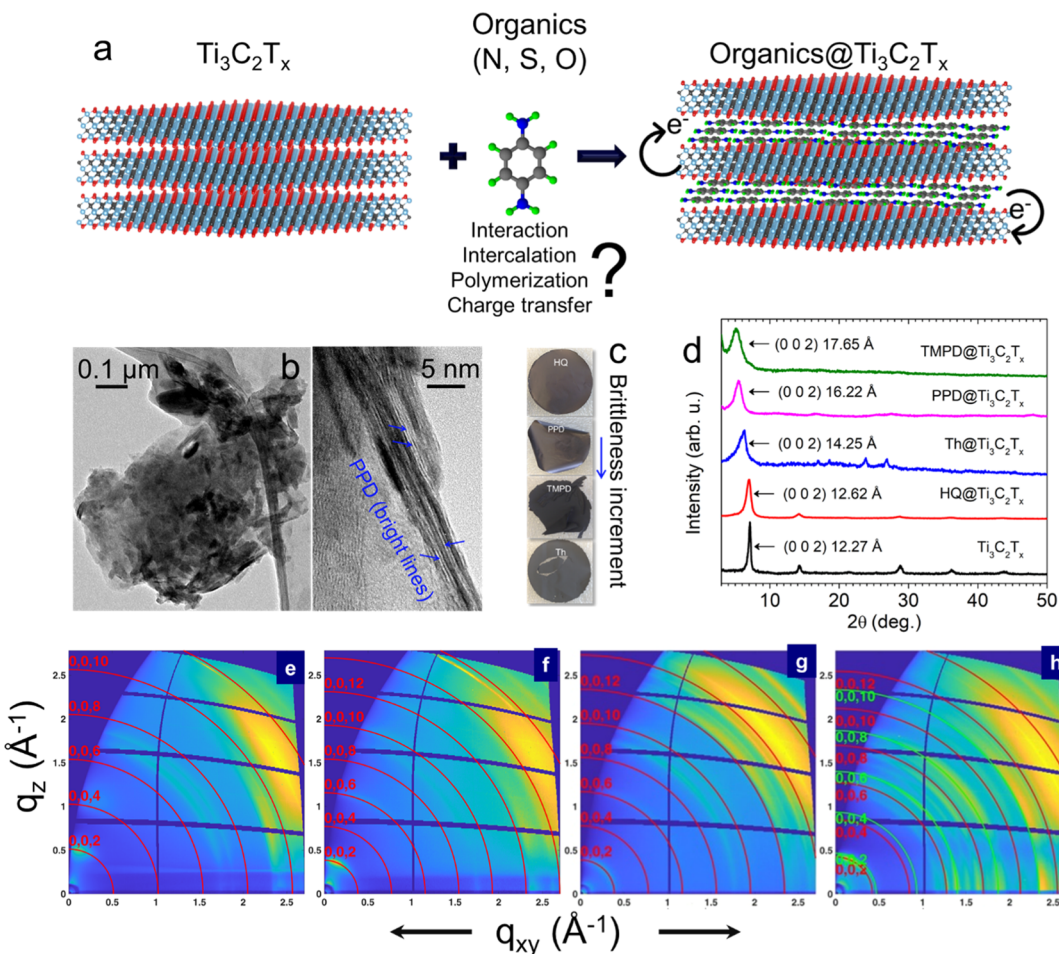


Figure 1. (a) Schematic illustration of various organic molecule interactions with $\text{Ti}_3\text{C}_2\text{T}_x$ MXene layers. Selected organic molecules have the same aromatic ring but differ based on their end group element (N, S, O, and tertiary-N-containing molecules). (b) Low-magnification TEM image shows the PPD-covered $\text{Ti}_3\text{C}_2\text{T}_x$ MXene flake (left) and the PPD@ $\text{Ti}_3\text{C}_2\text{T}_x$ film showing aligned organic layers (bright layers). (c) Digital photographs of the films based on physical mixing with colloidal suspension of $\text{Ti}_3\text{C}_2\text{T}_x$. Except HQ-treated MXene, all other films appeared relatively brittle. The increment in brittleness is marked with the arrow (d) XRD patterns of the pristine and organic molecule intercalated $\text{Ti}_3\text{C}_2\text{T}_x$ MXene films, showing the effect of the end group on c-LP expansion. GIDVis 2D, q -space indexed images from the DECTRIS detector of films of (e) HQ@ $\text{Ti}_3\text{C}_2\text{T}_x$, (f) PPD@ $\text{Ti}_3\text{C}_2\text{T}_x$, (g) TMPD@ $\text{Ti}_3\text{C}_2\text{T}_x$, and (h) Th@ $\text{Ti}_3\text{C}_2\text{T}_x$. The colors do not represent the intensity scale, which is properly shown in OP and IP profiles in Figure S1 (see the text). LP, geometry, pixel distance, and detector efficiency corrections applied.

amine, isopropylamine, and so forth) was intended to delaminate the MXene layers.^{3,5,12} In other cases, organic molecules (e.g., pyrrole, amino acids, and 3,4-ethylenedioxothiophene) were intercalated and unintentionally chemically reacted with the MXene surface to transform into other products.¹³ The majority of these studies relied on X-ray diffraction (XRD) to find changes in the c-lattice parameter (c-LP).^{3,5,12,13} However, understanding how organic molecules of different functionalities interact and whether their molecular network stay intact, how charge redistribution occurs upon intercalation, how the MXene local structure behaves, and how intercalant molecules enter and orientate in between the MXene layers are still the major questions that need to be answered.

Except few efforts,^{14,15} no systematic and well-characterized examples of organic–MXene heterostructures have been reported to date to address these questions. Without answering these fundamental questions, manufacturing of organic–MXene heterostructures with controlled chemical, physical, and/or electrochemical properties will be nearly impossible. Therefore, the emphasis of this study is to answer fundamental questions raised above. We used a combined experimental and theoretical

approach to understand the interactions of organic molecules of varying functional groups with MXene. To accomplish this goal, we selected four small organic molecules, namely, 1,4-benzenediol (HQ), 1,4-benzenedithiol (Th), 1,4-phenylenediamine (PPD), and *N,N,N',N'*-tetramethyl-*p*-phenylenediamine (TMPD), whose end groups are O, S, N, and tertiary amines, respectively. Among a variety of available MXenes, we selected $\text{Ti}_3\text{C}_2\text{T}_x$ MXene because it is the most studied MXene material to date.³

RESULTS AND DISCUSSION

Figure 1a shows the schematic of our approach to study the interaction mechanism of $\text{Ti}_3\text{C}_2\text{T}_x$ layers with small organic molecules having the same π -conjugated core but different end groups. Our choice of selected molecules was based on the fact that the majority of organic compounds have oxygen (O), nitrogen (N), sulfur (S), and/or amine functionalities that serve as the interaction sites, therefore studying their interaction/intercalation with MXene will provide a systematic guide to develop complex organic–MXene heterostructures. The molecular structures of the investigated molecules are provided in

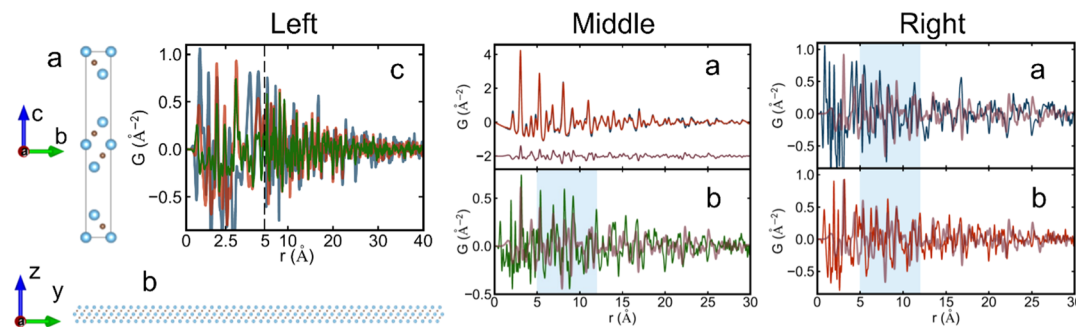


Figure 2. X-ray PDF analysis of heterostructures. (left, a) Structure of the crystalline Ti_3C_2 phase. (left, b) Structure of the single-layer Ti_3C_2 slab. The Ti and C atoms are in blue and brown in both (a,b), respectively. (left, c) Difference PDFs of Th@MXene, PPD@MXene, and HQ@MXene subtracting the pristine MXene are plotted in blue, red, and green curves, respectively. (middle, a) Simulated X-ray PDFs of the crystalline Ti_3C_2 bulk model (blue) and the single-layer slab model (red) are plotted together with their difference curve offset below in brown. (middle, b) Difference of HQ@MXene subtracting the pristine MXene is shown in green. The difference of the single-layer slab model subtracting the crystalline Ti_3C_2 bulk model is shown in brown. (right, a) Difference of Th@MXene subtracting the pristine MXene is shown in blue. (right, b) Difference of PPD@MXene subtracting the pristine MXene is shown in red. The difference of the slab subtracting the crystalline Ti_3C_2 model is shown in brown at both panels.

Figure S10. We mixed each organic molecule solution with the colloidal suspension of $\text{Ti}_3\text{C}_2\text{T}_x$ MXene in an optimized weight ratio of 2.4:1. It is important to mention that we have also tried multiple other ratios; however, we narrowed down this ratio for consistency throughout the article. After overnight mixing, filtered solutions gave free-standing organic–MXene films.

The low-magnification transmission electron microscopy (TEM) image of the PPD@ $\text{Ti}_3\text{C}_2\text{T}_x$ MXene flake (Figure 1b, left) and the cross-sectional TEM image (Figure 1b, right) of PPD@ $\text{Ti}_3\text{C}_2\text{T}_x$ show that the $\text{Ti}_3\text{C}_2\text{T}_x$ flake is covered with PPD and that the organic component is confined and aligned between the MXene sheets, respectively. All films were brittle, except the HQ-containing hybrid films (Figure 1c). TEM images in the Supporting Information (Figure S8) for pristine MXene and PPD@ $\text{Ti}_3\text{C}_2\text{T}_x$ hybrid further show that the $\text{Ti}_3\text{C}_2\text{T}_x$ MXene surface is clean; however, PPD@ $\text{Ti}_3\text{C}_2\text{T}_x$ is covered with the PPD.

XRD patterns (Figure 1d) of the heterostructure films showed that the end group of the organic molecule has a significant impact on the expansion of the *c*-LP of $\text{Ti}_3\text{C}_2\text{T}_x$ MXene, followed by the second-order (002) diffraction peaks. A small lengthening in the *c*-axis from 24.54 Å ($\text{Ti}_3\text{C}_2\text{T}_x$) to 25.23 Å was observed in the HQ@ $\text{Ti}_3\text{C}_2\text{T}_x$ film. On the contrary, such a shift was over 10 Å for the tertiary amine-containing hybrid film (i.e., TMPD@ $\text{Ti}_3\text{C}_2\text{T}_x$). Molecules with nitrogen-end (PPD) displayed ~8 Å lengthening compared to the pristine $\text{Ti}_3\text{C}_2\text{T}_x$ MXene film. Our systematic choice of molecules shows that the magnitude of *c*-LP expansion follows the nature of the end group of the organic molecules ($\text{O} < \text{S} < \text{primary N} < \text{tertiary N}$).

Furthermore, the study on grazing incidence XRD using synchrotron radiation of thin films of all considered heterostructures consistently confirms the above considerations. In fact, the 2D images are shown in Figure 1e–h—while extracted out-of-plane (OP) and in-plane (IP) profiles are shown in Figure S1—where also the indexing of the main diffraction arcs is shown. It can be noted that a general incomplete registration of the [0 0 *l*] reflection can be noted, as shown in Table S1. In spite of a high degree of order observed in the films, the peak width is larger than that measured for $\text{Ti}_3\text{C}_2\text{T}_x$ in powders,¹⁶ suggesting a limited coherence size along with either the *c* or *a* axis of the known hexagonal unit cell. Calculated approximate values are lesser than 9 nm.¹⁷ A preferred orientation with the *c*-axis normal to the film plane is observed as expected, as well as the presence of (1 0 0) reflection in IP view. Profiles are provided in

Supporting Information (Figure S1). The marked presence of large spots at $Q = 2.86 \text{ \AA}^{-1}$, attributed to reflections (1 0 *L*) particularly intense in the diagonal direction (45°), maps the partial orientation of crystallites bent with respect to the [0 0 *l*] crystallographic direction. In the HQ@ $\text{Ti}_3\text{C}_2\text{T}_x$ heterostructured film (Figure 1e), only three orders not well registered along the [0 0 *l*] direction are detected in the OP profile together with the (1 0 0) reflection in the IP profile, as well as the huge broad spot at $Q = 2.86 \text{ \AA}^{-1}$, attributed to (1 0 *L*) reflections. In view of a small increase of the *c*-axis (*c*-LP = 2.5 nm) with respect to $\text{Ti}_3\text{C}_2\text{T}_x$ and of the conservation of unit-cell characteristic of pure $\text{Ti}_3\text{C}_2\text{T}_x$, we can conclude that the intercalation of HQ molecules occurs as the usual cation impurities found in $\text{Ti}_3\text{C}_2\text{T}_x$ alone, strictly recalling the $\text{Ti}_3\text{C}_2\text{T}_x/\text{K}^+$ phase.¹⁶

In the PPD@ $\text{Ti}_3\text{C}_2\text{T}_x$ film (Figure 1f), six orders of the [001] directions are clearly detected with a noticeable level of registration, in fact, also the (0 0 14) reflection is attributed, while the (1 0 0) reflection is observed in IP only, indicating a marked orientation along the *c*-axis and a long-range order in the crystallites. Despite the orientation attained, the presence of (1 0 *L*) reflections at $Q = 2.86 \text{ \AA}^{-1}$ enforced in the diagonal direction (45°) is evidenced. The *c*-LP of 3.26 nm allows for the insertion of two layers of organic molecules among adjacent inorganic layers (see TEM Figure 1b, right), specifically in a model of π -stacked molecules accommodated inside the inorganic galleries. All in all, it can be concluded that a strong interaction between organic and inorganic components takes place.

In the TMPD@ $\text{Ti}_3\text{C}_2\text{T}_x$ heterostructure films (Figure 1g), three or four orders of the [0 0 *l*] direction, largely unregistered, are observable together with other peaks attributed to (1 0 0) and the convolution of (1 0 *L*) reflections at $Q = 2.86 \text{ \AA}^{-1}$, enhanced in the diagonal direction (45° in the 2D image). These observations suggest a reduced orientation of the heterostructure crystallite in the film. Finally, the *c*-LP increase (*c* = 3.5 nm) allows for the insertion in $\text{Ti}_3\text{C}_2\text{T}_x$ galleries of molecules or layers in an edge-on configuration. For Th@ $\text{Ti}_3\text{C}_2\text{T}_x$ (Figure 1h), the film could be considered as a pressed powder rather than a real film. A series of rings are observable, as expected in the case of a powder sample. For this reason, in Figure S1d only the OP profile is shown, and a huge number of diffraction effects could be detected whose indexing implies the co-presence of two different phases, although with noticeable unregistration along with [0 0 *l*]. The first one is related to a new Th@ $\text{Ti}_3\text{C}_2\text{T}_x$ ¹⁸ hybrid, while the second one is close to the $\text{Ti}_3\text{C}_2\text{T}_x$ -cation.¹⁶

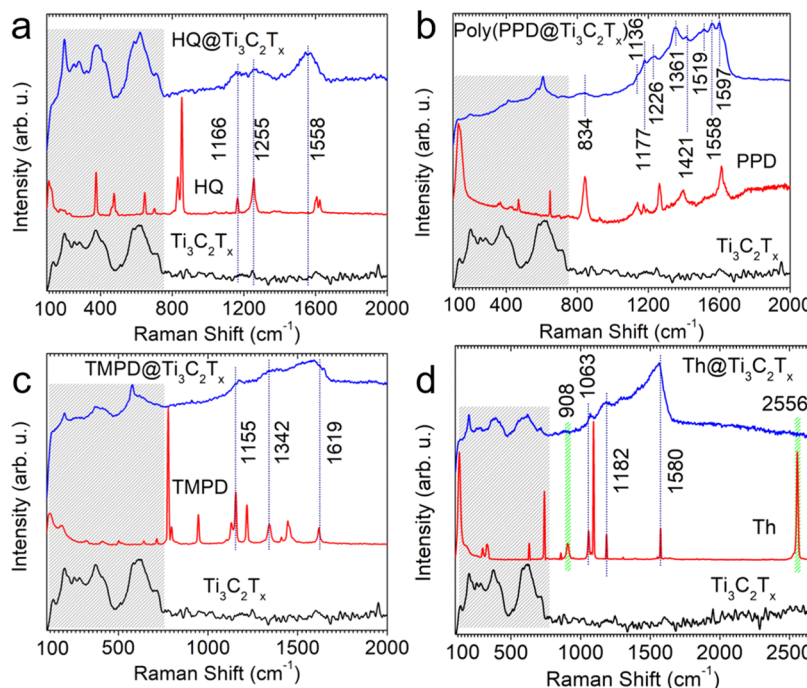


Figure 3. Raman spectra of organic molecules@ $\text{Ti}_3\text{C}_2\text{T}_x$ films: (a) $\text{Ti}_3\text{C}_2\text{T}_x$ film (below, black line), hydroquinone, HQ, (middle, red line), and HQ@ $\text{Ti}_3\text{C}_2\text{T}_x$ (up, blue line). (b) $\text{Ti}_3\text{C}_2\text{T}_x$ film (below, black line), PPD (middle, red line), and PPD@ $\text{Ti}_3\text{C}_2\text{T}_x$ (up, blue line). (c) $\text{Ti}_3\text{C}_2\text{T}_x$ film (below, black line), TMPD (middle, red line), and TMPD@ $\text{Ti}_3\text{C}_2\text{T}_x$ (up, blue line). (d) $\text{Ti}_3\text{C}_2\text{T}_x$ film (below, black line), Th (middle, red line), and Th@ $\text{Ti}_3\text{C}_2\text{T}_x$ (up, blue line).

The presence of odd terms in the $[0\ 0\ l]$ direction in both phases indicates the loose of hexagonal symmetry, possibly because of molecule incommensurability with respect to pure $\text{Ti}_3\text{C}_2\text{T}_x$ as well as misalignment of the inorganic layers, confirmed by the huge spot at $Q = 2.86 \text{ \AA}^{-1}$, particularly intense at 45° . The c-LP values (2.65 and ~ 2.9 nm, respectively) are compatible with the insertion of only a single layer of organic molecules, irrespective of the configuration assumed, that is, flat onto the layer or standing up. Such data consistently indicate the coexistence of different interacting organic– $\text{Ti}_3\text{C}_2\text{T}_x$ phases inside the galleries; namely, the first typical of π -stack linkage, while second of more strong interaction, for example, thiophene molecules bridging the adjacent metallic layers.

To track intercalation-induced structural changes in the hybrid films, we further investigated the changes in the X-ray pair distribution functions (PDFs) (Figure 2). We subtracted all the three organic@MXene PDFs from the HF-etched MXene sample, considering nearly similar PDFs with LiF + HCl MXene (see Supporting Information Figure S2 and relevant details), and the residuals are plotted in Figure 2 left, c.

Differences are evident between the different curves in the lower region ($r < 5 \text{ \AA}$), reflecting the different structures of the organic compounds themselves. However, in the higher r -ranges, the difference signals from the different organics have rather small signals that are quite like each other. This indicates, first, that the intercalation of different organic components changes the MXene structure by only a small amount but, second, changes it in the same way for all the different organics. Differences in the MXene PDF could reflect changes in the intralayer or interlayer correlations on intercalation or both. The most likely changes would be to the interlayer correlations and we first test this hypothesis. For example, we might expect that adding organics to the interlayer galleries will increase turbostratic disordering. The pristine MXenes are already

significantly turbostratically disordered.¹⁶ Nonetheless, we investigated the possibility that the degree of turbostratic disordering is changing on intercalation. To test this, we first extracted the signal in the PDF that originates from the interlayer correlations by subtracting the PDF of a single-layer slab model from the PDF of a fully ordered crystalline model (see Figure 2 left, b, and Supporting Information for more details). The simulated PDFs of both models are shown in Figure 2 (middle, a) and the difference curve, which shows the features in the PDF coming from the interlayer correlations, is plotted offset below. We then compared this difference signal with the difference signals from the measured organic intercalated versus pristine PDFs.

A representative of these plots, from the HQ@MXene case, is reproduced in Figure 2 (middle, b) and the others are in Figure 2 (right, a, b). By visual inspection, we see different behavior in three regions. Below $r = 5 \text{ \AA}$, the two difference curves are not so similar. This is expected because the HQ@MXene-pristine difference contains the signal from the organic, which is not in the slab-crystalline model's difference curve in this region. In the region $5 < r < 12 \text{ \AA}$, the two difference curves do appear to be highly similar. Finally, for $r > 12 \text{ \AA}$, the difference curves again do not correspond. The region $5 < r < 12 \text{ \AA}$ of the PDF contains interlayer correlations between the neighboring layers. The similarity between these two difference curves in this region might suggest that the pristine MXene has some degree of interlayer correlations between the adjacent layers, but not between the layers separated by a greater distance. The intercalation of the organics removes any residual stacking order that may have existed in the pristine MXene. One outcome of the current modeling would suggest that the structure of pristine MXene is not fully explained by a model with no stacking disorder,¹⁶ but rather there is a very limited amount of structural coherence between the nearest neighbor layers that

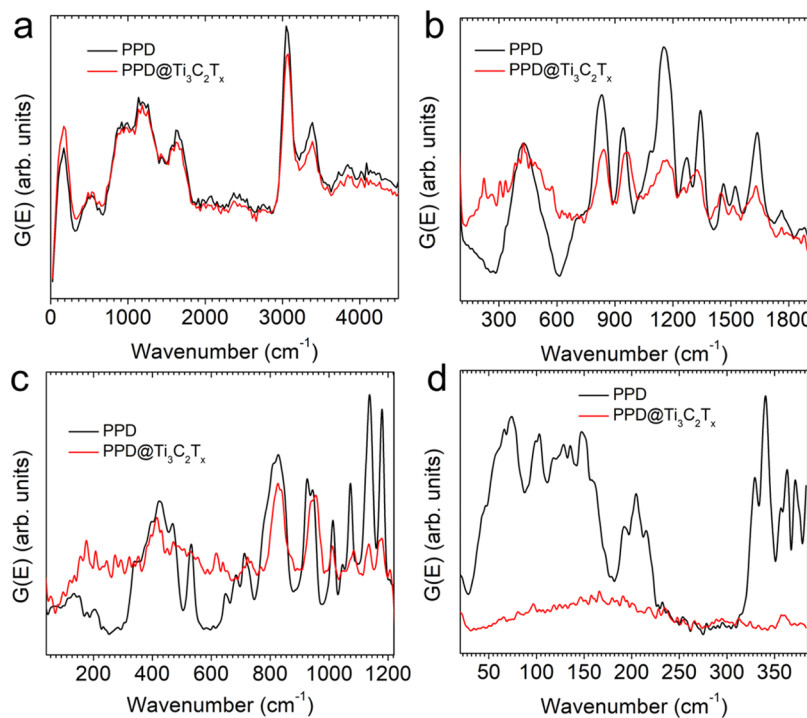


Figure 4. INS spectra of PPD and PPD@ $\text{Ti}_3\text{C}_2\text{T}_x$ obtained using (a) 600, (b) 250, (c) 160, and (d) 50 meV incident neutrons. All measurements were carried out at 6 K. For comparison with the IR data, neutron energy transfer is converted from meV to cm^{-1} .

gets removed by intercalation. Finally, we note that there is no evidence that the intralayer structure becomes modified on intercalation with the organics.

Functional groups of $\text{Ti}_3\text{C}_2\text{T}_x$ MXene such as $-\text{OH}$, $-\text{O}$, and $-\text{F}$ play an important role in the interactions with organic molecules.¹⁸ The interactions between the organic molecules and $\text{Ti}_3\text{C}_2\text{T}_x$ MXene can be divided into two broad categories: physical and chemical interactions.¹⁹ The nature of the interactions between organic species and MXene terminations is strongly end group-dependent. We have shown previously that polar organic molecules with charged nitrogen-containing ends interact strongly compared to their nonpolar counterparts via weak physical interactions.¹⁵ We also reported that amino acids (glycine) bind to the Ti atoms of the $\text{Ti}_3\text{C}_2\text{T}_x$ MXene, observed by the shared electron accumulation between the N and Ti atoms.¹⁹ Considering the presence of the hydrogen/nitrogen and $-\text{OH}$, $-\text{O}$, and $-\text{F}$ termini of the investigated organic molecules and $\text{Ti}_3\text{C}_2\text{T}_x$ MXene, respectively, hydrogen bonding would likely be the leading interaction among other physical interactions.²⁰ When organic components are mixed with the $\text{Ti}_3\text{C}_2\text{T}_x$ MXene, they usually exhibit weak physical interactions at first such as hydrogen bonding, van der Waals forces, and/or π - π interactions.^{15,19}

We probed the effect of organic molecules on the structure and surface chemistry of $\text{Ti}_3\text{C}_2\text{T}_x$ by Fourier-transform infrared (FTIR) and Raman spectroscopies. We also used the inelastic neutron scattering (INS) technique, which allows probing hydrogen-containing materials and their vibrational modes over a wide range of frequencies.²¹ Moreover, INS can be used to examine the low-energy phonon modes and provides accessibility to the energy range (below 50 meV), which otherwise is not possible with its optical counterparts (infrared and Raman spectroscopies).²¹

The FTIR spectra of HQ and HQ@ $\text{Ti}_3\text{C}_2\text{T}_x$ (Figure S3a) showed few bands like HQ without a significant shift or the

appearance of any new peaks, which is likely due to some residual HQ molecules trapped between the MXene sheets. It is important to mention that the FTIR spectrum of the $\text{Ti}_3\text{C}_2\text{T}_x$ is featureless.¹⁵ The HQ showed bands at ~ 3225 , 1646, 1514, 1437, 1352, 1260, 1207, 1190, and 1095 cm^{-1} , which may correspond to O–H vibrations, C=O stretching, C=C stretching, CH₂ bending, CH₂ wagging, C–O stretching, C–OH stretching, C–O stretching, and C–O–C stretching vibrations, respectively.^{22–26} HQ offered the tendency to form hydrogen bonding between hydroxyl groups of the quinone and $\text{Ti}_3\text{C}_2\text{T}_x$ MXene surface functional groups. The INS spectra measured using high energy neutrons (600 meV, Figure S4) for the pristine HQ and HQ@ $\text{Ti}_3\text{C}_2\text{T}_x$ showed a shift of the C–H stretching mode of the HQ@ $\text{Ti}_3\text{C}_2\text{T}_x$ sample ($\sim 3015 \text{ cm}^{-1}$) compared to HQ ($\sim 3076 \text{ cm}^{-1}$). The high-energy shoulder at $\sim 3266 \text{ cm}^{-1}$ is probably due to the O–H stretching mode and it is much broader in the intercalated sample, but this can also be due to the presence of the OH groups and/or water ($\sim 3427 \text{ cm}^{-1}$) in MXene.²⁷ Raman spectra of HQ, HQ@ $\text{Ti}_3\text{C}_2\text{T}_x$, and $\text{Ti}_3\text{C}_2\text{T}_x$ corroborated the FTIR and INS spectra. The Raman spectrum of HQ@ $\text{Ti}_3\text{C}_2\text{T}_x$ (Figure 3a) was dominated by the $\text{Ti}_3\text{C}_2\text{T}_x$ peaks with a few signature peaks from residual HQ appearing at ~ 1166 , 1255, and 1558 cm^{-1} .

In contrast to the HQ@ $\text{Ti}_3\text{C}_2\text{T}_x$ FTIR spectrum, PPD@ $\text{Ti}_3\text{C}_2\text{T}_x$ (Figure S3b) showed a different behavior, revealing new and broadened peaks. The bands in the PPD spectrum at ~ 3373 , 3301, and 3198 cm^{-1} are assigned to the N–H stretching modes of PPD.²⁸ The bands at ~ 1628 and 1513 cm^{-1} are assigned to C=N, C=C stretching vibrations in the phenazine structure, respectively.^{28,29} The ones at ~ 1310 and 1257 cm^{-1} are likely due to the C–N stretching of the PPD units.³⁰ The peaks at ~ 1122 and 823 cm^{-1} correspond to C–N stretching, and C–H OP bending vibrations.³¹ The new peaks at ~ 2923 and 2854 cm^{-1} are due to the asymmetric and stretching =CH₂ vibrations. The fact that these peaks are absent in PPD

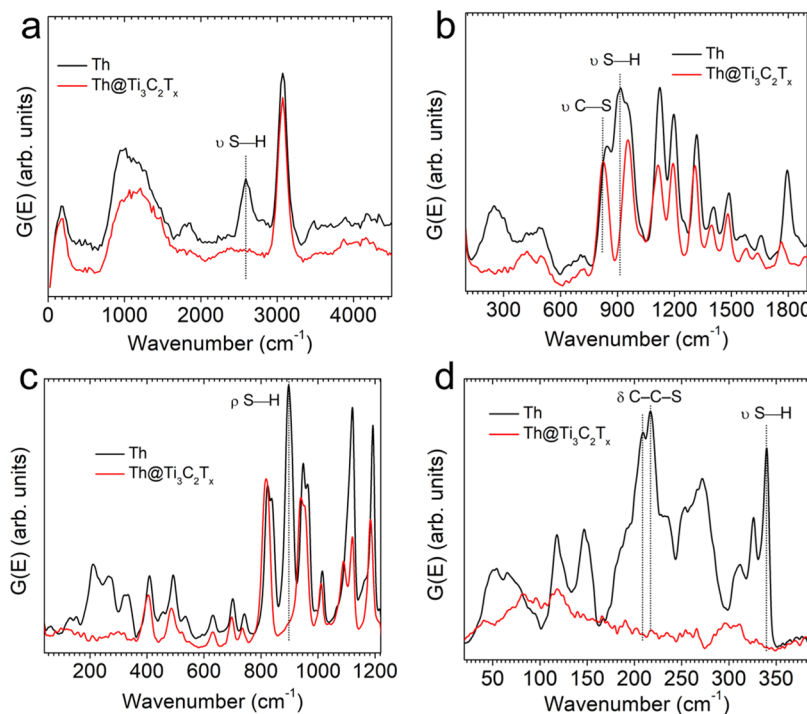


Figure 5. INS spectra of Th and Th@Ti₃C₂T_x obtained using (a) 600, (b) 250, (c) 160, and (d) 50 meV incident neutrons. All measurements were recorded at 6 K. For comparison with the IR data, neutron energy transfer is converted from meV to cm⁻¹.

may indicate that the PPD monomer units are linked together as shown previously when PPD was polymerized by conventional oxidative polymerization.³¹ The appearance of a new peak at ~1609 cm⁻¹ is ascribed to N—H deformation.³² The peak observed at ~1292 cm⁻¹ is related to the C—N stretching vibration of the benzenoid ring.³³ The band located at ~1106 cm⁻¹ indicates that the oligomeric/polymeric chains are doped (conductive).^{34,35} The peak at ~833 cm⁻¹ can be assigned to OP deformation of C—H groups.²⁹

The PPD@Ti₃C₂T_x Raman spectrum (Figure 3b) is dominated by the poly(PPD) peaks as reported previously based on the conventional oxidative polymerization of the PPD monomer.^{28,31,35–37} The peaks at ~1597, 1558, and 1519 cm⁻¹ are ascribed to C—C deformation of quinoid rings, C—C deformation of benzenoid rings, N—H bending deformation modes, respectively.^{36,37} The peaks at ~1421 and 1361 cm⁻¹ are attributed to the C—N⁺ stretching modes of the delocalized polaronic charge carriers.^{28,31} The peaks at ~1226, 1177, and 834 cm⁻¹ are attributed to the C—N stretching of polaronic units, quinoid ring vibrations, and deformative vibrations of the polymer amine groups, respectively.^{31,35,36} The INS spectra of PPD and PPD@Ti₃C₂T_x further confirmed the poly(PPD) formation (Figure 4). The intramolecular stretching N—H and C—H modes in the PPD and PPD@Ti₃C₂T_x spectra measured using high energy neutrons (600 meV) are almost unchanged (Figure 4a). There are slight modes changed in the range 1210–1700 cm⁻¹, confirming intermolecular interactions (Figure 4b, 250 meV).¹⁵ Then, modes around 828 and 927 cm⁻¹ are similar, but nearby modes at 1008, 1048, 1129, 1175 cm⁻¹ are strongly suppressed in PPD@Ti₃C₂T_x (Figure 4c, 160 meV).

The low-energy part of the spectra (Figure 4d) is changed strongly; the peaks at about 73, 103, 128–160, 204, 340, 363, and 371 cm⁻¹ in PPD transformed into the amorphous-like (dome-like) feature.³⁸ The intermolecular structure of the intercalated PPD probably strongly changed, more glass-like.³⁸

On the other hand, many examples of oxidative polymerization of PPD or tetramethyl substituted PPD are reported and according to the acidity of the medium, either polyquinoxaline or poly(1,4-benzoquinonediimine-N,N'-diyl 1,4-phenylene)—“pergranaline”—macromolecules are observed.³⁹ With regard to this, various catalytic systems,^{40,41} electrosynthesis,⁴¹ and intercalation in MoO₃⁴² have been exploited. Likely, PPD polymerization followed the polypyrrole formation on Ti₃C₂T_x MXene, where PPD molecules first interacted with the MXene surface terminations via physical interactions/adsorbed to the MXene surface, followed by the oxidation of the PPD monomer due to distinct acidic charter of the MXene.⁷ The oxidized PPD species then interacted with another PPD molecule to form a dimer, which subsequently undergoes further reaction with either oxidized/unoxidized PPD to form longer chains (chain propagation), which eventually get doped with the fluorine from the termination of the MXene layers.^{7,43}

FTIR bands of TMPD (Figure S3c) shown at ~2945 and 2874 cm⁻¹ are assigned to C—CH₃ stretching vibrations.^{15,44} The bands at ~2827 and 2780 cm⁻¹ are due to N—CH₃ vibrations in the TMPD ring.⁴⁴ Other TMPD bands were found at ~1612, 1517, 1314, 1211, 1175, 1127, 1055, 951, and 818 cm⁻¹, which can be ascribed to C=N vibrations, N—H bending vibrations, C—N stretching, C—C vibrations, C—N stretching vibration, C—H in-plane deformation, C—H vibrations, CH₂ rocking vibrations, and C—H OP bending vibrations, respectively.^{45–48} The hybrid FTIR spectrum of TMPD@Ti₃C₂T_x (Figure S3c) exhibited additional bands at ~2923, 2854, and 1557 cm⁻¹, which are assigned to asymmetrical C—H stretching vibrations, symmetrical C—H stretching, and N—H bending.^{45,46} The bands at ~1356, 1288, and 1314 cm⁻¹ are assigned to C—N stretching vibrations, respectively.^{45,49,50} The bands at ~1223 and 1165 cm⁻¹ are attributed to the stretching vibrations of C—N⁺• in the polaron

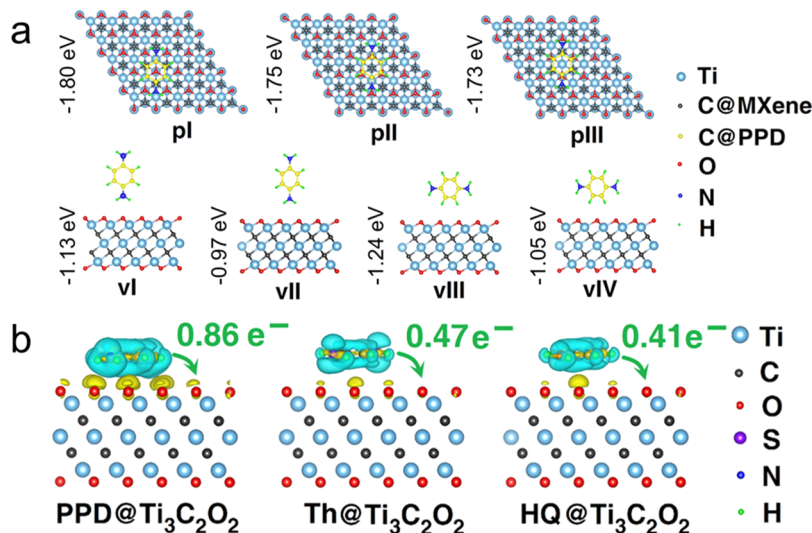


Figure 6. DFT calculations of heterostructures: (a) DFT-optimized geometries of PPD@Ti₃C₂T_x in various configurations. The binding energy of each configuration is mentioned on the left side of each optimized geometry. (b) Charge transfer from organic molecules of distinct end groups to Ti₃C₂O₂ (MXene).

structure and C—H bending vibration of the quinonoid ring, respectively.⁴⁹

TMMPD@Ti₃C₂T_x Raman spectrum (Figure 3c) showed shared peaks between TMMPD and Ti₃C₂T_x and did not show polymeric peaks like PPD. It is plausible for TMMPD just to react with the MXene surface but did not polymerize because of the methyl end groups which are less prone to initiate polymerization compared to the N—H groups of PPD. TMMPD@Ti₃C₂T_x showed broad peaks at 1152, 1342, and 1619 cm^{−1}, which can be ascribed to the TMMPD amine groups, C—N stretching, and C—C ring stretching, respectively.⁵¹ No significant change was noticed in high and intermediate energy INS spectra of the TMMPD and TMMPD@Ti₃C₂T_x (Figure S5a–c). The low-energy (<50 meV) spectra of the TMMPD-intercalated Ti₃C₂T_x looked like PPD (Figure S5d)—amorphous-like.³⁸ TMMPD would initially interact with the Ti₃C₂T_x-like PPD, but it would not form longer chain because it is difficult for the formed polaron ions to react with another TMMPD molecule, which gives rise to the polymerization. In this regard, the cell expansion >3.5 nm could be accomplished by means of the nonperiodic network formation of single-molecule layers, chemically linked to Ti₃C₂T_x inside the galleries.

Previously, we have noticed that pyrrole and 3,4-ethylenedioxothiophene upon mixing with Ti₃C₂T_x MXene spontaneously initiated oxidant-free polymerization that is in contrast to oxidant-based polymerization.^{7,19,43} A prerequisite for this polymerization was a charge transfer between the monomer and Ti₃C₂T_x MXene. For instance, a 0.34 electron transfer was needed to convert 3,4-ethylenedioxothiophene to poly(3,4-ethylenedioxothiophene).⁴³ Based on the density functional theory (DFT) calculations (see below), in addition to nearly 2 times higher binding energy (Figure S6) between PPD and Ti₃C₂T_x MXene (−1.8 eV), we found that a charge transfer of 0.86 occurs between PPD and MXene (Figure 6b, left), which is more than twice of 3,4-ethylenedioxothiophene (0.34), yet another evidence of the PPD polymerization.

The FTIR spectrum of Th exhibited very sharp peaks at ~2556, 1470, 1392, 1106, 1009, 905, and 808 cm^{−1}, which are assigned to S—H vibration, C—C ring stretching, C—H bending vibration, aryl ring vibrations, benzene thiol vibrations, S—H

vibration, and C—H OP bending modes, respectively (Figure S3d).^{52–55} Fermi resonance was observed for 1106 and 808 cm^{−1} bands. The absence of S—H vibration bands at ~2556 and 905 cm^{−1} in the Th@Ti₃C₂T_x spectrum gives hint that S—H groups may have broken, presumably because of the catalytic reactions with Ti₃C₂T_x intrinsic chemistry.^{7,14} Notably, the absence of S—H peaks at 908 and 2556 cm^{−1} (marked green, Figure 3d) in the Raman spectrum of Th@Ti₃C₂T_x further corroborated the FTIR spectroscopy results.

We further confirmed the local dissociation of the S—H bond using INS. In the high-energy INS spectra (600 meV, Figure 5a), the peak at ~3070 cm^{−1} is attributed to the C—H stretching modes, which have not changed upon Th intercalation in Ti₃C₂T_x MXene.⁵⁶ Peak at ~2589 cm^{−1} is attributed to the stretching S—H modes, this peak is absent in the Th—MXene;^{53,57} also, a strong peak at ~1846 cm^{−1} in Th is strongly decreased and shifts to a lower energy in the Th@Ti₃C₂T_x spectrum. Instead of three peaks in Th between 800 and 990 cm^{−1}, there are only two peaks in the Th@Ti₃C₂T_x spectrum (160 meV, Figure 5c).^{53,57} Notably, the S—H vibration band at ~909 cm^{−1} is vanished at both the 250 and 160 meV spectra (160 meV, Figure 5c).^{53,57} The bands at ~180–340 cm^{−1} in the low-energy part of spectra of Th are almost absent in the Th@Ti₃C₂T_x spectrum, as well as the peaks around 60, 120, and 140 cm^{−1} (Figure 5d). Importantly, a sharp band of S—H vibrations at 340 cm^{−1} in the Th@Ti₃C₂T_x spectrum is absent too—similar to the high-energy INS spectra.⁵⁸

From all optical spectroscopic measurements, the evidence is mounting for S—H dissociation from Th upon mixing with Ti₃C₂T_x MXene. Previously, the breaking of S—H bonds from Th on gold, silver, and other metals has been reported.⁵⁹ Here, the mechanism of S—H dissociation in the MXene surface is likely that Th first intercalated between Ti₃C₂T_x MXene (Figure 1d), followed by its adsorption (Figures 6a and S6), interaction (Figures S3d, 3d, 5, and S6), and charge transfer (Figure 6, middle) that resulted in the thiolate linkage formed with the Ti₃C₂T_x sheets by eliminating hydrogen from the S—H termini.⁶⁰

DFT calculations were further used to gain fundamental understanding of adsorption, interaction, and charge-transfer

mechanisms. We used PPD as a model system to explore the preferential orientation mechanism of these organic molecules on $\text{Ti}_3\text{C}_2\text{T}_x$ MXene in detail. We first tried to understand the PPD adsorption mechanism on the surface of $\text{Ti}_3\text{C}_2\text{O}_2$. We considered seven different configurations (Figure 6a), where p (I, II, III) and v (I, II, III, IV) refer to parallel and vertical orientations, respectively. The binding energies (BEs) E_{BE} of PPD or other organic molecules on the surface of $\text{Ti}_3\text{C}_2\text{O}_2$ are calculated using the following relation

$$E_{\text{BE}} = E_{\text{MXene+organic}} - (E_{\text{MXene}} + E_{\text{organic}})$$

where $E_{\text{MXene+organic}}$, E_{MXene} , and E_{organic} are the total energy of MXene with adsorbed organic molecules, the total energy of MXene, and the total energy of the organic molecule, respectively.

A smaller BE shows stronger interaction of PPD molecules with MXene (Figure 6a). Based on the calculated BE, which are shown with each DFT-optimized geometry, it turned out that parallel configurations are much stable than their vertical counterpart (Figure 6a). With the lowest binding energy of -1.8 eV, pI appeared as the most stable configuration for the PPD.

Based on these findings, we further explored the adsorption mechanism of Th and HQ molecules in three parallel configurations on MXene (Figure S6). For both Th and HQ, the most stable configurations with lowest BEs were pI, resulting in the BE values of -1.22 and -1.05 eV, respectively. However, these values are higher than BEs of the PPD case, confirming that PPD has a better affinity toward the MXene surface. From our DFT calculations, the order of interaction strength between MXene and organic molecules having end groups of O, S, and N is found to be N > S > O, which is like the order of experimental intercalation (Figure 1d).

To elucidate the origin of the strong interaction between organic molecules and MXene, we calculated the charge transfer using Bader analysis (Figure 6b).⁶¹ We found that there were 0.86, 0.47, and 0.41 electrons transferred from PPD, Th, and HQ to $\text{Ti}_3\text{C}_2\text{O}_2$, respectively. A high number of electron exchanges from PPD to MXene may be a strong reason for polymerization of PPD in the absence of oxidants.^{7,19,43} The amount of charge transfer followed the strength of BEs and intercalation between the MXene layers (i.e., N > S > O).

Redox-active organic molecules are known to boost the capacitance of the supercapacitors from several decades.⁶² For example, HQ, PPD, and TMPD have greatly improved the capacitance when coupled with carbon nanomaterials.^{63,64} As pristine $\text{Ti}_3\text{C}_2\text{T}_x$ MXene is an outstanding pseudocapacitive electrode (~ 1500 F/cm³, 450 F/g),⁶⁵ we wanted to push the limits further. We also wanted to understand how does charge storage vary at the MXene interface compared to carbons. The charge storage performance of the as-produced heterostructure films ($\sim 13\text{--}15$ μm) was tested in a three-electrode configuration in 3 M H₂SO₄ (Figure S7). All films showed pseudocapacitive behavior with pronounced redox peaks of $\text{Ti}_3\text{C}_2\text{T}_x$ MXene mainly because of the change in the titanium oxidation state.⁶⁵ Unlike carbon nanomaterials where boost in capacitance is seen at low scan rates,⁶³ the MXene interface behaved differently. The intercalated samples showed better capacitance only at higher scan rates because of the expanded layers where ions can move freely at high scan rates.⁶⁵ Only HQ-based films showed slightly better capacitance at a lower scan rate of 20 mV/s than their pristine counterpart likely because of their rapid redox reactions in protic electrolytes.⁶³ Nevertheless, the effect of interlayer spacing on capacitance was mostly seen at

high scan rates. The different behavior of the MXene interface compared to carbon nanomaterials toward redox-active organic molecules is likely due to a variety of interactions (discussed above) that play an important role in electrochemical charge storage. Therefore, we emphasize that understanding of interactions between the organic molecules and MXene is of utmost importance when creating MXene–organic heterostructures for electrochemical energy storage and other applications.

CONCLUSIONS

The growth in the field of MXene–organic heterostructures is hampered by the poor understanding of the reactive surface chemistry of MXenes with organic materials. We selected four model organic molecules, namely, HQ, Th, PPD, and TMPD, whose end groups are O, S, N, and tertiary amines, respectively. XRD patterns confirmed that the end group elements of the organic molecules dictate the change in the c-LP of the $\text{Ti}_3\text{C}_2\text{T}_x$ MXene. HQ having oxygen as the end groups appeared to be the least reactive with the $\text{Ti}_3\text{C}_2\text{T}_x$ MXene. In contrast to HQ, PPD intercalated more between the MXene layers, interacted, and polymerized to poly(PPD) without using any oxidant. This is opposed to conventional oxidative polymerization in which expensive and hazardous oxidants are used to initiate the polymerization. Low-energy neutron spectra further confirmed that PPD exhibited an amorphous-like feature and that the intermolecular structure of the PPD is strongly changed, more glass like. This polymerization is induced by strong binding of PPD with $\text{Ti}_3\text{C}_2\text{T}_x$ MXene (-1.8 eV) and charge transfer of the 0.86 electrons from the PPD to $\text{Ti}_3\text{C}_2\text{T}_x$ MXene as noted in our DFT calculations. Like PPD, TMPD-intercalated films also showed signals for the TMPD interaction with the MXene; however, we did not observe a strong signal for the polymerization in the Raman spectrum of TMPD@ $\text{Ti}_3\text{C}_2\text{T}_x$. From the range of optical and INS spectroscopies, we concluded that the S–H bond in Th is dissociated upon simple mixing with $\text{Ti}_3\text{C}_2\text{T}_x$ MXene because of the catalytic behavior of MXene. The mechanism of this dissociation seems to be that first Th molecules were intercalated between the $\text{Ti}_3\text{C}_2\text{T}_x$ MXene layers, followed by adsorption/interaction, and charge transfer from Th to MXene that resulted in thiolate linkage formed with the $\text{Ti}_3\text{C}_2\text{T}_x$ sheets by eliminating hydrogen from the S–H termini. First-principles calculations confirmed that organic molecules lie flat to the MXene surface confirmed by the lowest binding of these configurations. DFT calculations further confirmed that the binding strength of the organic molecules is end group-dependent and increases, like the order of intercalation seen in the XRD diffractograms. From Bader analysis, we confirmed that 0.86, 0.47, and 0.41 electrons transferred from PPD, Th, and HQ to $\text{Ti}_3\text{C}_2\text{T}_x$ MXene, respectively. The order of charge transfer followed the order of BE and intercalation between $\text{Ti}_3\text{C}_2\text{T}_x$ MXene layers. The nature of the interactions between $\text{Ti}_3\text{C}_2\text{T}_x$ MXene and investigated organic compounds is largely dependent on the interacting molecules, which makes it complex to generalize the nature of interactions for the $\text{Ti}_3\text{C}_2\text{T}_x$ MXene and organic molecules. Combining the redox-active organic molecules with the MXene interface did not positively impact the charge storage performance at low scan rates because of the interactions/transformations of organics at the $\text{Ti}_3\text{C}_2\text{T}_x$ MXene surface/interface. Better capacitance at higher scan rates was recorded, which is due to pillarizing of organics between the $\text{Ti}_3\text{C}_2\text{T}_x$ MXene layers, resulting in better charge mobility. The detailed results presented in this study may guide the synthesis

of new MXene–organic heterostructures with controlled properties for a broad range of applications.

■ ASSOCIATED CONTENT

SI Supporting Information

The Supporting Information is available free of charge at <https://pubs.acs.org/doi/10.1021/acs.chemmater.0c02662>.

Experimental details, OP and IP XRD profiles extracted from 2D images of the MXene–organic films, X-ray PDF analysis of heterostructures, FTIR spectra of organic molecules@ $Ti_3C_2T_x$ films, inelastic neutron spectra of organic molecules@ $Ti_3C_2T_x$ films, DFT-optimized most stable configurations of heterostructures, and electrochemical performance ([PDF](#))

■ AUTHOR INFORMATION

Corresponding Author

Muhammad Boota — *A. J. Drexel Nanomaterials Institute and Department of Materials Science and Engineering, Drexel University, Philadelphia, Pennsylvania 19104, United States;* [ORCID iD](https://orcid.org/0000-0001-9855-4295); Email: boota@drexel.edu

Authors

Chi Chen — *A. J. Drexel Nanomaterials Institute and Department of Materials Science and Engineering, Drexel University, Philadelphia, Pennsylvania 19104, United States; School of Optical and Electronic Information, Huazhong University of Science and Technology, Wuhan, Hubei 430074, People's Republic of China;* [ORCID iD](https://orcid.org/0000-0003-2479-9657)

Long Yang — *Department of Applied Physics and Applied Mathematics, Columbia University, New York, New York 10027, United States;* [ORCID iD](https://orcid.org/0000-0001-8731-0172)

Alexander I. Kolesnikov — *Neutron Scattering Division, Oak Ridge National Laboratory, Oak Ridge, Tennessee 37830, United States;* [ORCID iD](https://orcid.org/0000-0003-1940-4649)

Naresh C. Osti — *Neutron Scattering Division, Oak Ridge National Laboratory, Oak Ridge, Tennessee 37830, United States;* [ORCID iD](https://orcid.org/0000-0002-0213-2299)

William Porzio — *Institute of Chemical Sciences and Technologies "G.Natta" Consiglio Nazionale delle Ricerche (SCI-TEC), 20133 Milano, Italy;* [ORCID iD](https://orcid.org/0000-0001-6151-6199)

Luisa Barba — *Istituto di Cristallografia-Sincrotrone Elettra, Trieste 34149, Italy*

Jianjun Jiang — *School of Optical and Electronic Information, Huazhong University of Science and Technology, Wuhan, Hubei 430074, People's Republic of China;* [ORCID iD](https://orcid.org/0000-0001-9178-8988)

Complete contact information is available at:

<https://pubs.acs.org/doi/10.1021/acs.chemmater.0c02662>

Notes

The authors declare no competing financial interest.

■ ACKNOWLEDGMENTS

We thank Prof. Yury Gogotsi and Prof. Simon J. L. Billinge for the helpful discussion and advice. This work was supported as part of the Fluid Interface Reactions, Structures, and Transport (FIRST) Center, an Energy Frontier Research Center funded by the U.S. Department of Energy, Office of Science, and Office of Basic Energy Sciences. C.C. was supported by the Chinese Scholarship Council. L.Y.'s effort on PDF analysis and modeling

was supported by the NSF MRSEC program through Columbia in the Center for Precision Assembly of Superstratic and Superatomic Solids (DMR-1420634). X-ray PDF measurements were conducted on beamline 28-ID2 of the National Synchrotron Light Source II (NSLSII), a U.S. Department of Energy (DOE) Office of Science User Facility operated for the DOE Office of Science by Brookhaven National Laboratory under Contract no. DE-SC0012704. Use of the beamline X17A of the NSLS was supported by the DOE-BES under contract no. DEAC02-98CH10886. This research used resources at the Spallation Neutron Source, a DOE Office of Science User Facility operated by the Oak Ridge National Laboratory. Oak Ridge National Laboratory is managed by UT-Battelle, LLC, for the U.S. DOE under Contract no. DEAC05-00OR22725.

■ REFERENCES

- (1) Novoselov, K. S.; Mishchenko, A.; Carvalho, A.; Castro Neto, A. H. 2D Materials and van Der Waals Heterostructures. *Science* **2016**, *353*, aac9439.
- (2) Gobbi, M.; Orgiu, E.; Samori, P. When 2D Materials Meet Molecules: Opportunities and Challenges of Hybrid Organic/Inorganic van Der Waals Heterostructures. *Adv. Mater.* **2018**, *30*, 1706103.
- (3) Naguib, M.; Kurtoglu, M.; Presser, V.; Lu, J.; Niu, J.; Heon, M.; Hultman, L.; Gogotsi, Y.; Barsoum, M. W. Two-Dimensional Nanocrystals Produced by Exfoliation of Ti_3AlC_2 . *Adv. Mater.* **2011**, *23*, 4248–4253.
- (4) Gogotsi, Y.; Anasori, B. The Rise of MXenes. *ACS Nano* **2019**, *13*, 8491–8494.
- (5) Anasori, B.; Lukatskaya, M. R.; Gogotsi, Y. 2D Metal Carbides and Nitrides (MXenes) for Energy Storage. *Nat. Rev. Mater.* **2017**, *2*, 16098.
- (6) Shahzad, F.; Alhabeb, M.; Hatter, C. B.; Anasori, B.; Man Hong, S.; Koo, C. M.; Gogotsi, Y. Electromagnetic Interference Shielding with 2D Transition Metal Carbides (MXenes). *Science* **2016**, *353*, 1137–1140.
- (7) Boota, M.; Anasori, B.; Voigt, C.; Zhao, M.-Q.; Barsoum, M. W.; Gogotsi, Y. Pseudocapacitive Electrodes Produced by Oxidant-Free Polymerization of Pyrrole between the Layers of 2D Titanium Carbide (MXene). *Adv. Mater.* **2015**, *28*, 1517–1522.
- (8) Hantanasisirakul, K.; Zhao, M.-Q.; Urbankowski, P.; Halim, J.; Anasori, B.; Kota, S.; Ren, C. E.; Barsoum, M. W.; Gogotsi, Y. Fabrication of $Ti_3C_2T_x$ MXene Transparent Thin Films with Tunable Optoelectronic Properties. *Adv. Electron. Mater.* **2016**, *2*, 1600050.
- (9) Zhang, J.; Zhao, Y.; Guo, X.; Chen, C.; Dong, C.-L.; Liu, R.-S.; Han, C.-P.; Li, Y.; Gogotsi, Y.; Wang, G. Single Platinum Atoms Immobilized on an MXene as an Efficient Catalyst for the Hydrogen Evolution Reaction. *Nat. Catal.* **2018**, *1*, 985–992.
- (10) Sarycheva, A.; Polemi, A.; Liu, Y.; Dandekar, K.; Anasori, B.; Gogotsi, Y. 2D Titanium Carbide (MXene) for Wireless Communication. *Sci. Adv.* **2018**, *4*, No. eaau0920.
- (11) Kim, S. J.; Koh, H.-J.; Ren, C. E.; Kwon, O.; Maleski, K.; Cho, S.-Y.; Anasori, B.; Kim, C.-K.; Choi, Y.-K.; Kim, J.; Gogotsi, Y.; Jung, H.-T. Metallic $Ti_3C_2T_x$ MXene Gas Sensors with Ultrahigh Signal-to-Noise Ratio. *ACS Nano* **2018**, *12*, 986–993.
- (12) Anasori, B.; Gogotsi, Y. *2D Metal Carbides and Nitrides (MXenes), Structure, Properties and Applications*; Springer: Berlin, 2019.
- (13) Boota, M. MXene–Organic Hybrid Materials. In *2D Metal Carbides and Nitrides (MXenes): Structure, Properties and Applications*; Anasori, B., Gogotsi, Y., Eds.; Springer International Publishing: Cham, 2019; pp 221–251.
- (14) Overbury, S. H.; Kolesnikov, A. I.; Brown, G. M.; Zhang, Z.; Nair, G. S.; Sacci, R. L.; Lotfi, R.; van Duin, A. C. T.; Naguib, M. Complexity of Intercalation in MXenes: Destabilization of Urea by Two-Dimensional Titanium Carbide. *J. Am. Chem. Soc.* **2018**, *140*, 10305–10314.
- (15) Boota, M.; Pasini, M.; Galeotti, F.; Porzio, W.; Zhao, M.-Q.; Halim, J.; Gogotsi, Y. Interaction of Polar and Nonpolar Polyfluorenes

- with Layers of Two-Dimensional Titanium Carbide (MXene): Intercalation and Pseudocapacitance. *Chem. Mater.* **2017**, *29*, 2731–2738.
- (16) Shi, C.; Beidaghi, M.; Naguib, M.; Mashtalar, O.; Gogotsi, Y.; Billinge, S. J. L. Structure of Nanocrystalline Ti_3C_2 MXene Using Atomic Pair Distribution Function. *Phys. Rev. Lett.* **2014**, *112*, 125501.
- (17) Porzio, W.; Scavia, G.; Barba, L.; Arrighetti, G.; McNeill, C. R. On the Packing and the Orientation of P(NDI2OD-T2) at Low Molecular Weight. *Eur. Polym. J.* **2014**, *61*, 172–185.
- (18) Meng, F.; Seredych, M.; Chen, C.; Gura, V.; Mikhailovsky, S.; Sandeman, S.; Ingavle, G.; Ozulumba, T.; Miao, L.; Anasori, B.; Gogotsi, Y. MXene Sorbents for Removal of Urea from Dialysate: A Step toward the Wearable Artificial Kidney. *ACS Nano* **2018**, *12*, 10518–10528.
- (19) Chen, C.; Boota, M.; Urbankowski, P.; Anasori, B.; Miao, L.; Jiang, J.; Gogotsi, Y. Effect of Glycine Functionalization of 2D Titanium Carbide (MXene) on Charge Storage. *J. Mater. Chem. A* **2018**, *6*, 4617–4622.
- (20) Xu, Q.; Yang, W.; Wen, Y.; Liu, S.; Liu, Z.; Ong, W.-J.; Li, N. Hydrochromic Full-Color MXene Quantum Dots through Hydrogen Bonding toward Ultrahigh-Efficiency White Light-Emitting Diodes. *Appl. Mater. Today* **2019**, *16*, 90–101.
- (21) Dutta, R.; Rao, M. N.; Kumar, A. Investigation of Ionic Liquid Interaction with ZnBDC-Metal Organic Framework through Scanning EXAFS and Inelastic Neutron Scattering. *Sci. Rep.* **2019**, *9*, 14741.
- (22) Ramachandran, R.; Saranya, M.; Velmurugan, V.; Raghupathy, B. P. C.; Jeong, S. K.; Grace, A. N. Effect of Reducing Agent on Graphene Synthesis and Its Influence on Charge Storage towards Supercapacitor Applications. *Appl. Energy* **2015**, *153*, 22–31.
- (23) Kaviyarasu, K.; Manikandan, E.; Paulraj, P.; Mohamed, S. B.; Kennedy, J. One Dimensional Well-Aligned CdO Nanocrystal by Solvothermal Method. *J. Alloys Compd.* **2014**, *593*, 67–70.
- (24) Balaji, S. S.; Sathish, M. Supercritical Fluid Processing of Nitric Acid Treated Nitrogen Doped Graphene with Enhanced Electrochemical Supercapacitance. *RSC Adv.* **2014**, *4*, 52256–52262.
- (25) Basu, P.; Repanas, A.; Chatterjee, A.; Glasmacher, B.; NarendraKumar, U.; Manjubala, I. PEO–CMC Blend Nanofibers Fabrication by Electrospinning for Soft Tissue Engineering Applications. *Mater. Lett.* **2017**, *195*, 10–13.
- (26) Boota, M.; Hatzell, K. B.; Alhabeb, M.; Kumbur, E. C.; Gogotsi, Y. Graphene-Containing Flowable Electrodes for Capacitive Energy Storage. *Carbon* **2015**, *92*, 142–149.
- (27) Kolesnikov, A. I.; Anovitz, L. M.; Mamontov, E.; Podlesnyak, A.; Ehlers, G. Strong Anisotropic Dynamics of Ultra-Confining Water. *J. Phys. Chem. B* **2014**, *118*, 13414–13419.
- (28) Yang, S.; Liu, D.; Liao, F.; Guo, T.; Wu, Z.; Zhang, T. Synthesis, Characterization, Morphology Control of Poly(p-Phenylenediamine)- Fe_3O_4 Magnetic Micro-Composite and Their Application for the Removal of $Cr_2O_7^{2-}$ from Water. *Synth. Met.* **2012**, *162*, 2329–2336.
- (29) Min, Y.-L.; Wang, T.; Zhang, Y.-G.; Chen, Y.-C. The Synthesis of Poly(p-Phenylenediamine) Microstructures without Oxidant and Their Effective Adsorption of Lead Ions. *J. Mater. Chem.* **2011**, *21*, 6683–6689.
- (30) Liu, Z.; Zhou, H.; Huang, Z.; Wang, W.; Zeng, F.; Kuang, Y. Graphene Covalently Functionalized with Poly(p-Phenylenediamine) as High Performance Electrode Material for Supercapacitors. *J. Mater. Chem. A* **2013**, *1*, 3454–3462.
- (31) Jaidev, J.; Ramaprabhu, S. Poly(p-Phenylenediamine)/Graphene Nanocomposites for Supercapacitor Applications. *J. Mater. Chem.* **2012**, *22*, 18775–18783.
- (32) Mehdipour-Ataei, S.; Sarrafi, Y.; Hatami, M.; Akbarian-Feizi, L. Poly(Sulfone Ether Amide Amide)s as a New Generation of Soluble, Thermally Stable Polymers. *Eur. Polym. J.* **2005**, *41*, 491–499.
- (33) Xing, S.; Zheng, H.; Zhao, G. Preparation of Polyaniline Nanofibers via a Novel Interfacial Polymerization Method. *Synth. Met.* **2008**, *158*, 59–63.
- (34) Sharma, S.; Nirikhe, C.; Pethkar, S.; Athawale, A. a. Chloroform Vapour Sensor Based on Copper/Polyaniline Nanocomposite. *Sens. Actuators, B* **2002**, *85*, 131–136.
- (35) Boota, M.; Paranthaman, M. P.; Naskar, A. K.; Li, Y.; Akato, K.; Gogotsi, Y. Waste Tire Derived Carbon-Polymer Composite Paper as Pseudocapacitive Electrode with Long Cycle Life. *ChemSusChem* **2015**, *8*, 3576–3581.
- (36) Wang, J.-J.; Jiang, J.; Hu, B.; Yu, S.-H. Uniformly Shaped Poly(p-Phenylenediamine) Microparticles: Shape-Controlled Synthesis and Their Potential Application for the Removal of Lead Ions from Water. *Adv. Funct. Mater.* **2008**, *18*, 1105–1111.
- (37) Zhang, T.; Yang, S.; Sun, J.; Li, X.; He, L.; Yan, S.; Kang, X.; Hu, C.; Liao, F. Poly(p-Phenylenediamine) Fluorescent Nanosphere: A Ultra-Sensitive Fluorescent Probe for Caffeine. *Synth. Met.* **2013**, *181*, 86–91.
- (38) Inoue, K.; Kanaya, T.; Ikeda, S.; Kaji, K.; Shibata, K.; Misawa, M.; Kiyanagi, Y. Low-energy Excitations in Amorphous Polymers. *J. Chem. Phys.* **1991**, *95*, 5332–5340.
- (39) Durgaryan, A. A.; Arakelyan, R. A.; Durgaryan, N. A. Oxidative Polymerization of P-Phenylenediamine. *Russ. J. Gen. Chem.* **2014**, *84*, 1095–1100.
- (40) Čirić-Marjanović, G.; Marjanović, B.; Bober, P.; Rozlívková, Z.; Stejskal, J.; Trčková, M.; Prokeš, J. The Oxidative Polymerization of P-Phenylenediamine with Silver Nitrate: Toward Highly Conducting Micro/Nanostructured Silver/Conjugated Polymer Composites. *J. Polym. Sci. Part A Polym. Chem.* **2011**, *49*, 3387–3403.
- (41) Amer, I.; Brandt, S. Synthesis and Characterization of Poly(p-Phenylenediamine) and Its Derivatives Using Aluminium Triflate as a Co-Catalyst. *Cogent Eng.* **2018**, *5*, 1499701.
- (42) Guan, H.; Fan, L.-Z.; Zhang, H.; Qu, X. Polyaniline Nanofibers Obtained by Interfacial Polymerization for High-Rate Supercapacitors. *Electrochim. Acta* **2010**, *56*, 964–968.
- (43) Chen, C.; Boota, M.; Xie, X.; Zhao, M.; Anasori, B.; Ren, C. E.; Miao, L.; Jiang, J.; Gogotsi, Y. Charge Transfer Induced Polymerization of EDOT Confined between 2D Titanium Carbide Layers. *J. Mater. Chem. A* **2017**, *5*, 5260–5265.
- (44) Lin-Vien, D.; Colthup, N. B.; Fateley, W. G.; Grasselli, J. G. *CHAPTER 10-Compounds Containing -NH₂, -NHR, and -NR₂ Groups-The Handbook of Infrared and Raman Characteristic Frequencies of Organic Molecules*; Academic Press: San Diego, 1991; pp 155–178.
- (45) Gerwert, K.; Souvignier, G.; Hess, B. Simultaneous Monitoring of Light-Induced Changes in Protein Side-Group Protonation, Chromophore Isomerization, and Backbone Motion of Bacteriorhodopsin by Time-Resolved Fourier-Transform Infrared Spectroscopy. *Proc. Natl. Acad. Sci. U.S.A.* **1990**, *87*, 9774–9778.
- (46) Fatiadi, A. J. Infrared Absorption Spectra of 2-Oxo-1,3-Bis(Phenylhydrazone) Derivatives and Related Bis- and Tris-Phenylhydrazones. *J. Res. Natl. Bur. Stand., Sect. A* **1967**, *71*, 277–285.
- (47) Kubinyi, M.; Varsányi, G.; Grofcsik, A. Vibrational Study of N,N,N',N'-Tetramethyl-p-Phenylenediamine and Its Radical Cation. *Spectrochim. Acta, Part A* **1980**, *36*, 265–272.
- (48) Sun, M.; Zhang, S.; Jiang, T.; Zhang, L.; Yu, J. Nano-Wire Networks of Sulfur-Polyppyrrole Composite Cathode Materials for Rechargeable Lithium Batteries. *Electrochim. Commun.* **2008**, *10*, 1819–1822.
- (49) Sedénková, I.; Trčková, M.; Stejskal, J. Thermal Degradation of Polyaniline Films Prepared in Solutions of Strong and Weak Acids and in Water – FTIR and Raman Spectroscopic Studies. *Polym. Degrad. Stab.* **2008**, *93*, 2147–2157.
- (50) Verma, D.; Dutta, V. Role of Novel Microstructure of Polyaniline-CSA Thin Film in Ammonia Sensing at Room Temperature. *Sens. Actuators, B* **2008**, *134*, 373–376.
- (51) Wang, X.; Shao, M.; Shao, G.; Wu, Z.; Wang, S. A Facile Route to Ultra-Long Polyaniline Nanowires and the Fabrication of Photoswitch. *J. Colloid Interface Sci.* **2009**, *332*, 74–77.
- (52) McFarland, A. D.; Young, M. A.; Dieringer, J. A.; Van Duyne, R. P. Wavelength-Scanned Surface-Enhanced Raman Excitation Spectroscopy. *J. Phys. Chem. B* **2005**, *109*, 11279–11285.
- (53) Kestell, J.; Abuflaha, R.; Garvey, M.; Tysoe, W. T. Self-Assembled Oligomeric Structures from 1,4-Benzenedithiol on Au(111) and the Formation of Conductive Linkers between Gold Nanoparticles. *J. Phys. Chem. C* **2015**, *119*, 23042–23051.

- (54) Sturrock, E. J.; Chen, Q.; Borchardt, P. H.; Richardson, N. V. Coverage Dependent Change in Orientation for the Adsorption of Benzyl Mercaptan on Au(111). *J. Electron Spectrosc. Relat. Phenom.* **2004**, *135*, 127–134.
- (55) Yang, W.; Zhang, Y.-R.; Yuen, A. C.-Y.; Chen, T. B.-Y.; Chan, M.-C.; Peng, L.-Z.; Yang, W.-J.; Zhu, S.-E.; Yang, B.-H.; Hu, K.-H.; Yeoh, G.-H.; Lu, H.-D. Synthesis of Phosphorus-Containing Silane Coupling Agent for Surface Modification of Glass Fibers: Effective Reinforcement and Flame Retardancy in Poly(1,4-Butylene Terephthalate). *Chem. Eng. J.* **2017**, *321*, 257–267.
- (56) Bae, S. J.; Lee, C.-r.; Choi, I. S.; Hwang, C.-S.; Gong, M.-s.; Kim, K.; Joo, S.-W. Adsorption of 4-Biphenylisocyanide on Gold and Silver Nanoparticle Surfaces: Surface-Enhanced Raman Scattering Study. *J. Phys. Chem. B* **2002**, *106*, 7076–7080.
- (57) Joo, S. W.; Han, S. W.; Kim, K. Adsorption of 1,4-Benzeneedithiol on Gold and Silver Surfaces: Surface-Enhanced Raman Scattering Study. *J. Colloid Interface Sci.* **2001**, *240*, 391–399.
- (58) Parker, S. F. Assignment of the Vibrational Spectrum of L-Cysteine. *Chem. Phys.* **2013**, *424*, 75–79.
- (59) Matsuhita, R.; Horikawa, M.; Naitoh, Y.; Nakamura, H.; Kiguchi, M. Conductance and SERS Measurement of Benzenedithiol Molecules Bridging Between Au Electrodes. *J. Phys. Chem. C* **2013**, *117*, 1791–1795.
- (60) Kestell, J.; Abuflaha, R.; Garvey, M.; Tysoe, W. T. Self-Assembled Oligomeric Structures from 1,4-Benzeneedithiol on Au(111) and the Formation of Conductive Linkers between Gold Nanoparticles. *J. Phys. Chem. C* **2015**, *119*, 23042–23051.
- (61) Bader, R. F. *Atoms in Molecules: A Quantum Theory*; Clarendon Press, 1990.
- (62) MacDiarmid, A. G.; Kaner, R. B. *Handbook of Conducting Polymers*; Marcel Dekker, 1986; Vol. 1.
- (63) Boota, M.; Hatzell, K. B.; Kumbur, E. C.; Gogotsi, Y. Towards High Energy Density Pseudocapacitive Flowable Electrodes via Incorporation of Hydroquinone. *ChemSusChem* **2015**, *8*, 835–843.
- (64) Boota, M.; Chen, C.; Bécuwe, M.; Miao, L.; Gogotsi, Y. Pseudocapacitance and Excellent Cyclability of 2,5-Dimethoxy-1,4-Benzoquinone on Graphene. *Energy Environ. Sci.* **2016**, *9*, 2586–2594.
- (65) Lukatskaya, M. R.; Kota, S.; Lin, Z.; Zhao, M.-Q.; Shpigel, N.; Levi, M. D.; Halim, J.; Taberna, P.-L.; Barsoum, M. W.; Simon, P.; Gogotsi, Y. Ultra-High-Rate Pseudocapacitive Energy Storage in Two-Dimensional Transition Metal Carbides. *Nat. Energy* **2017**, *2*, 17105.